Supplementary information: Variation of thermal conductivity and heat flux at the Earth's core mantle boundary

M. W. Ammann, A. M. Walker, S. Stackouse,
J. Wookey, A. M. Forte, J. P. Brodholt and D. P. Dobson

January 3, 2014

1 Single crystal thermal conductivity

The methodology used to calculate the thermal conductivity of single crystal $MgSiO_3$ perovskite and post-perovskite is described in the main text. Further results are presented below.

In Tables 1 and 2 we report the cell parameters of perovskite and post-perovskite as a function of pressure and temperature using the two pairs of interatomic potentials. These results, which were derived from equilibrium molecular dynamics (MD), are used to set the cell parameters for the non-equilibrium molecular dynamics (NEMD) used to evaluate the thermal conductivity (the NEMD calculations must be performed at fixed cell parameters). Discrepancies between the cell parameters of the two sets of interatomic potentials are larger for post-perovskite than perovskite but even these differences are acceptable (1-2%) given the limitations of any simple parameterised model.

Table 3 gives the thermal conductivities as a function of pressure and temperature calculated from NEMD simulations using the two pairs of potentials. These results are also represented graphically in the main text. A parameterisation of these results (given in the main text) are used to calculate the heat flux as described below.

1.1 Comparison with DFT simulations

Figure 1 compares the results of the two interatomic potentials with the results from density functional theory (DFT). Both show good agreement with DFT, however, the extrapolations to infinite cell-size differ in terms of the resulting anisotropy. Nevertheless, DFT and interatomic potentials give on average the same values for the thermal conductivity. DFT data points shown in Figure 5 in the main text were previously presented[1] and will form the basis for a future publication.

Table 1: Equations of state for perovskite (PV) and post-perovskite (PPV) using the interatomic potentials of Murakami et al.[2]

Pressure	1000 K			2000 K			3000 K			4000 K		
PPV	a [Å]	b [Å]	c [Å]	a [Å]	b [Å]	c [Å]	a [Å]	b [Å]	c [Å]	a [Å]	b [Å]	c [Å]
120 GPa	2.4632	8.3555	6.1022	2.4752	8.3462	6.1297	2.4824	8.3811	6.1417	2.4897	8.4369	6.1569
140 GPa	2.4436	8.2714	6.0523	2.4546	8.2588	6.0772	2.4602	8.2980	6.0861	2.4690	8.3294	6.1055
PV												
20 GPa	4.6772	4.8112	6.7863	4.7482	4.8492	6.7935	4.7682	4.8897	6.8439	-	-	-
130 GPa	4.3625	4.5340	6.3310	4.3868	4.5466	6.3317	4.3882	4.5490	6.3764	-	-	-

Table 2: Equations of state for perovskite (PV) and post-perovskite (PPV) using the interatomic potentials of Oganov et al.[3]

Pressure	1000 K			2000 K			3000 K			4000 K		
PPV	a [Å]	b [Å]	c [Å]	a [Å]	b [Å]	c [Å]	a [Å]	b [Å]	c [Å]	a [Å]	b [Å]	c [Å]
120 GPa	2.5210	8.2648	6.0274	2.5333	8.2492	6.0673	2.5486	8.2420	6.0938	2.5580	8.2949	6.1043
140 GPa	2.5026	8.1541	5.9868	2.5131	8.1360	6.0203	2.5248	8.1380	6.0448	2.5334	8.1833	6.0556
PV												
20 GPa	4.7281	4.8342	6.8221	4.7708	4.8685	6.8653	4.8293	4.9169	6.9070	-	-	-
130 GPa	4.3807	4.5192	6.3236	4.4003	4.5244	6.3438	4.4203	4.5347	6.3691	-	-	-

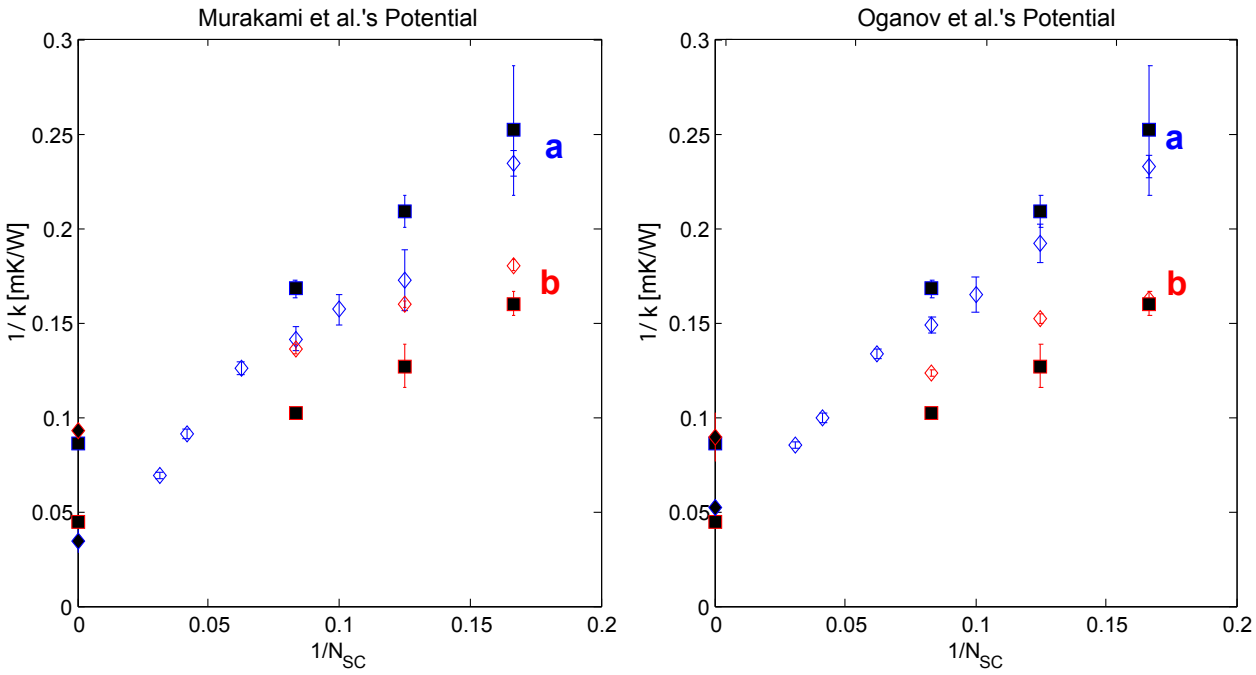

Figure 1: Comparison of results from interatomic potentials with those from DFT as a function of the simulation-cell length. Empty diamonds are interatomic potentials, filled squares are DFT values, red is the thermal conductivity along b, blue along a. Values at 0 are the extrapolations to infinite cell size.

Table 3: Thermal conductivities (κ in W/mK, with formally propagated errors) of perovskite (PV) and post-perovskite (PPV) along the three crystallographic axes (a, b and c) using the interatomic potentials of Murakami et al.[2] and Oganov et al.[4]. κ_{11}, κ_{22} and κ_{33} are the thermal conductivities along the a, b and c axes, respectively. The other three components of the single crystal thermal conductivity tensor are zero by symmetry for these orthorhombic crystals.

Pressure	1000 K			2000 K			3000 K			4000 K		
PPV	k_{11}	k_{22}	k_{33}	k_{11}	k_{22}	k_{33}	k_{11}	k_{22}	k_{33}	k_{11}	k_{22}	k_{33}
Murakami et al.[2]												
120 GPa	40.1±6.1	20.0±1.3	26.7±1.4	25.4±2.9	12.5±2.0	15.7±0.8	19.3±1.6	10.7±1.5	11.4±0.9	11.8±0.3	9.7±0.8	10.4±0.8
140 GPa	38.6±5.8	26.6±4.4	30.6±2.1	22.9±2.1	15.6±0.9	17.9±1.4	19.8±1.3	13.8±0.7	14.4±1.1	12.8±0.8	9.4±0.9	11.4±0.5
Oganov et al.[4]												
120 GPa	32.0±3.9	25.2±2.5	22.2.0±0.7	18.7±1.2	16.8±1.4	12.9±0.7	13.8±1.0	13.1±0.8	11.4±0.7	9.9±0.5	10.5±0.4	9.6±0.8
140 GPa	33.1±0.8	28.3±1.5	22.8±1.1	18.5±0.7	17.2±1.0	14.0±1.1	13.2±0.6	14.1±0.3	11.8±0.4	11.4±0.6	10.4±0.5	9.5±0.3
PV												
Murakami et al.[2]												
20 GPa	9.4±1.0	-	11.4±0.7	6.2±0.2	-	7.3±0.5	5.8±0.3	-	6.9±0.7	-	-	-
130 GPa	15.7±0.8	-	17.6±0.6	11.0±0.8	-	12.0±0.9	9.1±0.7	-	10.7±0.5	-	-	-
Oganov et al.[4]												
20 GPa	8.8±0.4	-	9.7±0.7	6.0±0.2	-	7.0±0.5	5.1±0.2	-	6.4±0.5	-	-	-
130 GPa	14.1±1.0	-	20.2±0.6	10.2±0.6	-	11.7±0.8	8.3±0.3	-	9.9±0.5	-	-	-

2 From conductivity to heat flux

Geophysically, the thermal conductivity is of interest because it controls the movement of heat. Recall that, in three dimensions, the heat flux q_i in direction x_i is given by Fourier's law:

$$q_i = -K_{ij}\frac{dT}{dx_j}, \tag{2.1}$$

where K is the second order thermal conductivity tensor and T is the temperature. The repeated index on the right hand side implies a summation for values $j = 1, 3$. This simple equation can produce counterintuitive results and we explore some of these in simple worked example in Section 2.1. In order to calculate the heat flux across the thermal boundary layer above the CMB we therefore need to combine two models: one for the thermal conductivity of the rock forming the lowermost mantle and one for its temperature.

We evaluate the heat flux on a 5° by 5° grid using models of the thermal conductivity and temperature field described below. Our model of the thermal conductivity can include the effect of texture (see Section 2.3) and we compare models with and without texturing. We evaluate the three components of the temperature gradient by finite difference of the temperature model described in Section 2.2. Summary information for all models of CMB heat flux are given in Table 4.

Table 4: Summary information and outline of all models of CMB heat flux

Model specification	Heat flux			
	Total (TW)	Maximum (W/m^2)	Mean (W/m^2)	Minimum (W/m^2)
Isotropic ppv with 1D temperature model	4.94			
Isotropic pv with 1D temperature model	3.48			
Fixed conductivity with variable temperature model, "10 W/mK" in Figure 3	3.80	0.053	0.025	-0.005
Isotropic ppv with variable temperature model, "Post-perovskite" in Figure 3	4.93	0.058	0.032	-0.005
Isotropic pv with variable temperature model, "Perovskite" in Figure 3	3.45	0.041	0.023	-0.005
Isotropic mixed phase, "Mixed phase" in Figure 3	4.83	0.058	0.032	-0.004
P100 texture, pure ppv, 1D temperature model, Figure 4	5.04	0.038	0.033	0.029
P010 texture, pure ppv, 1D temperature model, Figure 4	4.87	0.035	0.032	0.030
P001 texture, pure ppv, 1D temperature model, Figure 4	4.67	0.037	0.030	0.027
P100 texture, mixed phase, variable temperature model, Figure 5	4.90	0.061	0.032	-0.004
P010 texture, mixed phase, variable temperature model, Figure 5	4.82	0.057	0.032	-0.004
P001 texture, mixed phase, variable temperature model, Figure 5	4.65	0.056	0.031	-0.004

2.1 Anisotropic thermal conductivity: worked example

Fourier's law (Equation 2.1) will be familiar to most readers and is most easily remembered as the simple rule that heat cannot of itself pass from one body to a hotter body. However, for anisotropic thermal conductivity, Equation 2.1 can yield perfectly correct and meaningful results which are counter intuitive and potentially confusing. In this section we outline one

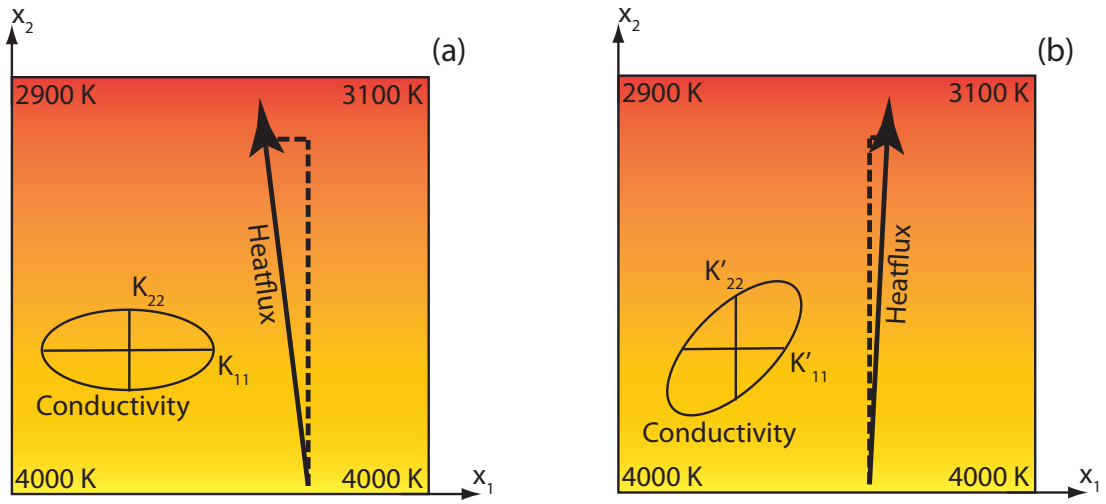

Figure 2: **Example of anisotropic conductivity.** Heat flux calculated for a simple box model as described in the text. The difference between (a), where the horizontal component of the heat flux vector is from right to left, and (b), where it is from left to right, is that the conductivity tensor is rotated by 45°. (Neither the conductivity tensor or heat flux vector are drawn to scale.)

case which illustrates this potential confusion. For simplicity our example is two-dimensional but the principal extends to three-dimensions without difficulty. We consider a box with large vertical temperature gradient and a small horizontal temperature gradient shown in Figure 2. When evaluated at the centre of the box, this setup gives temperature gradients $dT/dx_1 = 100$ and $dT/dx_2 = -1000$ (the positive x_2 direction is upwards). We then imagine the thermal conductivity in the box is anisotropic with conductivity in the low conductivity direction 80% of the conductivity in the high conductivity direction (which we take as 10 W/mK) and calculate the heat flux. Aligning the material with the low conductivity horizontal gives a conductivity tensor:

$$\mathsf{K} = \begin{pmatrix} 10 & 0 \\ 0 & 8 \end{pmatrix}, \tag{2.2}$$

and yields a heat flux of:

$$\mathbf{q} = \begin{bmatrix} -(10 \times 100) - (0 \times -1000) \\ -(0 \times 100) - (8 \times -1000) \end{bmatrix} = \begin{bmatrix} -1000 \\ 8000 \end{bmatrix}. \tag{2.3}$$

This is straightforward. Heat flows mostly upwards and slightly to the left, down the temperature gradient. The counterintuitive result arises if the material is rotated 45° anticlockwise about the origin. The thermal conductivity tensor expressed on the fixed frame of reference, K', is now given by:

$$\mathsf{K}' = \mathbf{R} \cdot \mathsf{K} \cdot \mathbf{R}^T, \tag{2.4}$$

where the rotation matrix $\mathbf{R}$ is just:

$$\mathbf{R} = \begin{pmatrix} \cos(45) & -\sin(45) \\ \sin(45) & \cos(45) \end{pmatrix}, \tag{2.5}$$

and $\mathbf{R}^T$, is its transpose. (An element-by-element version of Equation 2.4 is embedded in Equation 2.8, below.) The rotated conductivity tensor is then:

$$\mathsf{K}' = \begin{pmatrix} 9 & 1 \\ 1 & 9 \end{pmatrix}, \tag{2.6}$$

and we note in passing that the eigenvalues are still both positive (they are 10 and 8 by construction). The heat flux in this second arrangement is:

$$\mathbf{q} = \begin{bmatrix} -(9 \times 100) - (1 \times -1000) \\ -(1 \times 100) - (9 \times -1000) \end{bmatrix} = \begin{bmatrix} 100 \\ 8900 \end{bmatrix}. \tag{2.7}$$

Overall, heat still flows from the hot lower boundary to the cold upper boundary. However, counter intuitively if we just consider the horizontal component of the heat flux and the horizontal component of the temperature gradient we find that 100 W/m^2 is apparently conducted up the temperature gradient, from cold to hot. This is, of course, an illusion. Anisotropy means that while the heat still flows from the hotter to the colder, it no longer always flows from the hottest to the coldest. The heat flux vector need not be parallel to the steepest temperature gradient, and this has interesting consequences for heat flux in particular directions.

2.2 Temperature model

Our temperature model consists of two components, a one-dimensional geotherm and local temperature perturbations. The geotherm is taken from Stacey and Davis (Appendix G)[5] and based on a CMB temperature of 3739 K. This relatively low temperature for the CMB results in a low total CMB heat flux, but here we are interested in probing the patterns and causes of the spatial variation in heat flux, not the total energy budget of the core. We note that the value of the total heat flux is essentially controlled by the poorly determined radial temperature-gradients at the CMB (e.g., 4.85 K/km[5], 7.5 K/km[6]). Higher CMB heat fluxes are certainly possible (and seem increasingly likely) and we caution the reader that the integrated values shown below (Figures 3 – 5) are artefacts of an approach designed to probe lateral variation, and the absolute values are unconstrained in this work.

The major driving force for variations in the heat flux across the CMB is temperature variations in the mantle. Models of the geodynamo have made use of tomographic models of seismic wave speeds in the lowermost mantle to set a spatially varying CMB temperature and heat flux. However, temperature is not the only contribution to changes in wave speeds in the mantle and here me make use of a model that allows wave speeds to vary with temperature and composition. This is the TX2008 model used in Walker et al.[7] and based on the inversion of global S-wave travel times, the global gravity field, dynamic surface topography, tectonic plate motions, and of the excess ellipticity of the core–mantle boundary[8]. We note that the inversion is designed to minimise the misfit between the observations and model while minimising the

compositional variation (and thus maximising the effect of temperature). This means that we should tend to maximise the variation in heat flux across the CMB. We form a model of temperature (rather than temperature variation, which is approximately ±500 K) by shifting 1D temperature profile at each point according to the modelled temperature variation in the lowermost depth slice of the TX2008 model (covering the interval from a depth of 2650 km to the CMB - see Figure 3 of Walker et al.[7]).

We calculate thermal gradients by finite difference but expect the lateral thermal gradients to diminish (and radial gradients to increase) downwards, towards the CMB. To simplify the problem we assume conduction through a 150 km thick layer and evaluate the gradients 75 km above the CMB. When we allow perovskite or post-perovskite to co-exist in D″, we assign the conductivity of the majority phase in this layer. While this does not capture the intricate double crossing of the phase boundary expected in the pure system, smearing of the phase boundary in the presence of solid-solution between the phases will reduce the error associated with this approximation. The temperature perturbation field is slowly varying (degree 128) so we use a small (< 100 km) displacement and calculate gradients using central differencing. The radial gradient is calculated from the change in temperature between the fixed CMB temperature and the varying temperature 150 km above the CMB. Overall, assigning a constant thermal gradient for a thick layer will underestimate the radial gradient close to the CMB and overestimate it towards the top of the layer. The opposite is true for the radial gradients. The overall effect will be to reduce the CMB heat flux but, as each point is treated in an identical manner, lateral variations should be robust.

2.3 Polycrystalline thermal conductivity

Our atomic scale calculations yield k, the single crystal thermal conductivity tensor of perovskite and post-perovksite. In order to convert this into the thermal conductivity of a polycrystalline rock we need to know its composition and the orientation and location of the grains. The general problem is intractable because we do not have a full grain scale description of the lowermost mantle and even if we did the resulting numerical challenge would be extreme. Instead, we make use of approximate solutions for the aggregate thermal conductivity that include the effect of the distribution of crystal orientations but not their relative position. The simple starting point assumes that the crystals are randomly oriented giving an isotropic bulk conductivity. This is not sufficient to fully determine the bulk conductivity as the thermal gradient and heat flux both vary from grain to grain, but we can place limits on the conductivity of the aggregate conductivity[9]. The Voigt bound is derived from the assumption that the thermal gradient is identical everywhere in the aggregate (and thus the heat flux varies between individual, differently oriented, grains). For an aggregate consisting of orthorhombic crystals this is just given by the arithmetic mean of the single crystal conductivities along each crystallographic axis: $K = (k_{11} + k_{22} + k_{33})/3$. The assumption for the Reuss bound is that the heat flux is the same in each crystal (and the temperature gradient varies within the aggregate). This is equal to the harmonic mean of the three single-crystal conductivities: $K = 3/(k_{11}^{-1} + k_{22}^{-1} + k_{33}^{-1})$. The Reuss bound is therefore always equal to or lower than the Voigt bound and the difference between the two limits becomes larger as the anisotropy of thermal conductivity grows. For our simplest isotropic models of CMB heat flux, we make use of the isotropic Voigt thermal

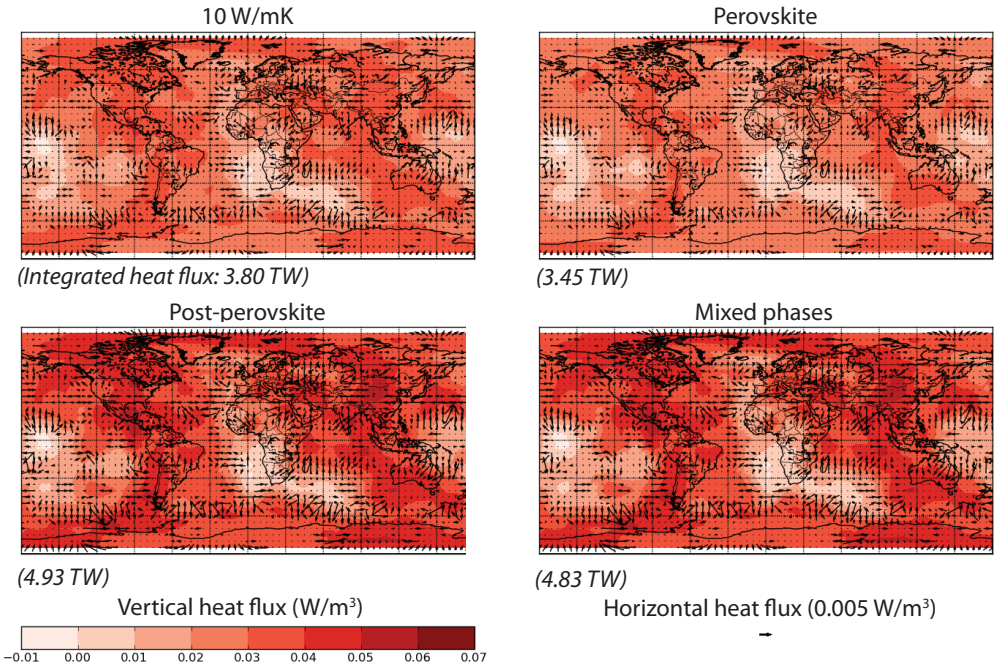

Figure 3: **CMB heat flux for various isotropic models of thermal conductivity in the lowermost mantle.** Coloured contours indicate the vertical component of the heat flux and the arrows indicate the horizontal component. All models make use of a model of temperature variation in the lowermost mantle describe in Section 2.2 and assume isotropic thermal conductivities. Labels indicate different models for conductivity: "10 W/mK" is a fixed conductivity independent of temperature (so the temperature gradient is the only control on heat flux), "Perovskite" and "Post-perovskite" use the isotropic Voigt average of the single crystal conductivities including the effect of temperate on thermal conductivity and "Mixed phases" assumes that hotter areas are composed of perovskite and colder areas composed of post-perovsktie (Section 2.2. Numbers in parentheses is the total vertical component of the CMB heat flux. The integrated heat flux is low compared to that determined by Stacey and Davis[5] because we do not account for a non-linear temperature profile through D''.

conductivity assuming either post-perovskite or perovskite controls conduction above the CMB (Figure 3) and examine how the heat flux varies spatially using the temperature model described below.

However, there is strong evidence from seismology that post-perovskite crystals in the lowermost mantle are not randomly oriented. Measured seismic anisotropy resolved by normal mode, tomographic, and shear-wave splitting studies are all consistent with the post-perovskite crystals being aligned by convective flow in the mantle. If this is the source of seismic anisotropy the same mechanism will produce anisotropic thermal conductivity in the bulk rock. In order to model this possibility we re-use the results of calculations where the elastic anisotropy was modelled using a description of current convective flow in the lowermost mantle to drive simulations of deformation and texture deformation. This approach is described fully in[7] but, briefly, we built a model of texture development in the lowermost mantle by tracing particle trajectories through a model of present day mantle flow derived from the joint inversion of

seismic and geodynamic observables[8,10,11]. Specifically, for the current work we use the flow field we previously described[7] as TX2008.V2. Velocity gradient tensors are collected along the particle paths and used to drive simulations of texture development as pieces of mantle material traverse the post-perovskite stability field. This approach yields a description of texture (described by the orientations of 500 individual crystal grains) on a grid above the CMB. We find the thermal conductivity of these anisotropic aggregates in much the same way as for the isotropic case described above except the Voigt and Reuss bounds on the conductivity tensor are now given by:

$$K_{ij}^{\text{Voigt}} = \frac{1}{500}\sum_{n=1}^{500} g_{ip}^n g_{jq}^n k_{pq} \quad \text{and} \quad K_{ij}^{\text{Reuss}} = \left[\frac{1}{500}\sum_{n=1}^{500} g_{ip}^n g_{jq}^n k_{pq}^{-1}\right]^{-1}, \tag{2.8}$$

where the 500 orientations are described by n rotation matrices denoted $\mathbf{g}^n$ and there is an implied summation over the repeated indices p and q.

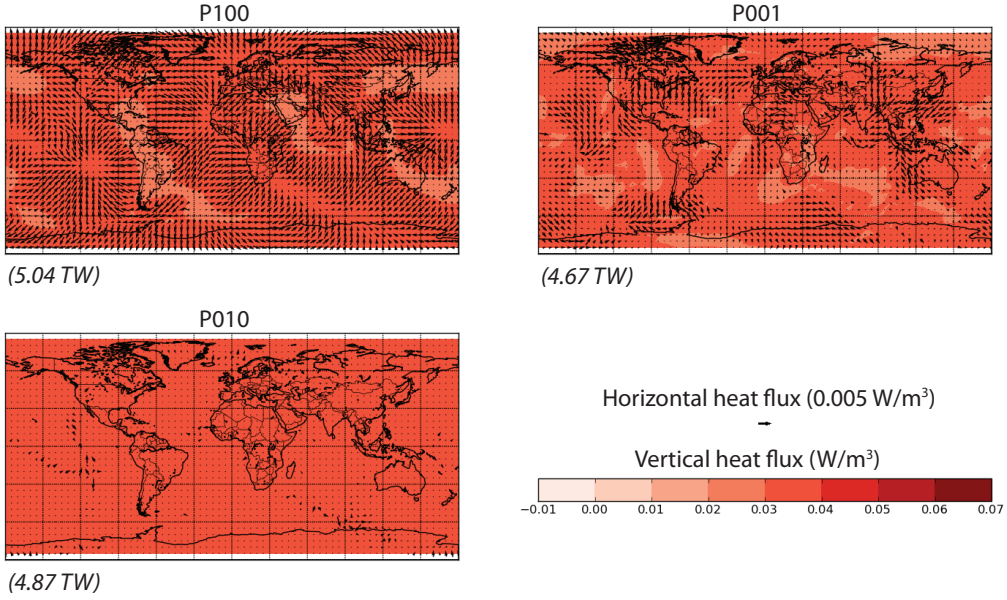

Figure 4: **CMB heat flux for various anisotropic models of thermal conductivity in a lowermost mantle of constant temperature.** Scale and symbols are identical to Figure 3 but the thermal conductivity is anisotropic and derived from three different models of the activities of post-perovskite slip systems. See text for details.

The model of texture development, which made use of the visco-plastic self-consistent homogenisation approach[12,13], requires a description of the way that single crystals deform by the motion of dislocations. For post-perovskite there is significant uncertainty in the literature as to the most active slip system, let alone the full details of the single crystal yield surface that is needed for these calculations. We therefore made use of three models of single crystal plasticity which are intended to cover the range of proposed processes. In particular, we make use of the parameters used by Merkel and co-workers[14] to explain the earliest experimental data which

favours deformation on the (100) and {110} glide planes, a model derived from Peierls-Nabarro modelling using density functional theory[15,16] which prefers slip on (010) , and a model intended to reproduce the recent experimental results of Miyagi et al.[17] in which deformation is dominantly accommodated by slip on (001). We call these models P100, P010 and P001, respectively. The heat flux for these three cases, where the spatial variation is only caused by anisotropic thermal conductivity, is shown in Figure 4.

A further consideration is that the dominant phase may vary laterally across the lowermost mantle with, potentially, post-perovskite only being found in colder regions and perovskite dominating the hotter regions of the D″. In order to study this possibility we take a simple approach and assume that in each point the heat flux is either controlled by the conductivity of either perovskite or post-perovskite depending if the location where the texture is evaluated is in the perovskite or post-perovskite stability field. More complex approaches are clearly possible including the possibility of double crossings of the phase boundary, but the evidence recently available from experiments, indicating thick two-phase regions and dramatic changes in the transition pressure with chemistry makes this approach troublesome. The simple approach taken here should serve to indicate the general trend for a mixed-phase lowermost mantle. If double crossing is significant then this will decrease the effect of introducing two phases as there will be more perovskite immediately above the CMB. To determine if we should assign a location the thermal conductivity of perovskite or post-perovskite we use a Clapeyron slope of 9.56 $MPaK^{-1}$ and a 0 K transition pressure of 98.7 GPa taken from DFT calculations on the pure $MgSiO_3$ phases[3] and the same temperature model as we use to set the thermal gradients and thermal conductivities (Section 2.2). The isotropic two-phase case is shown in Figure 3 while cases including the effect of both texture, temperature, and the phase transition are shown in Figure 5.

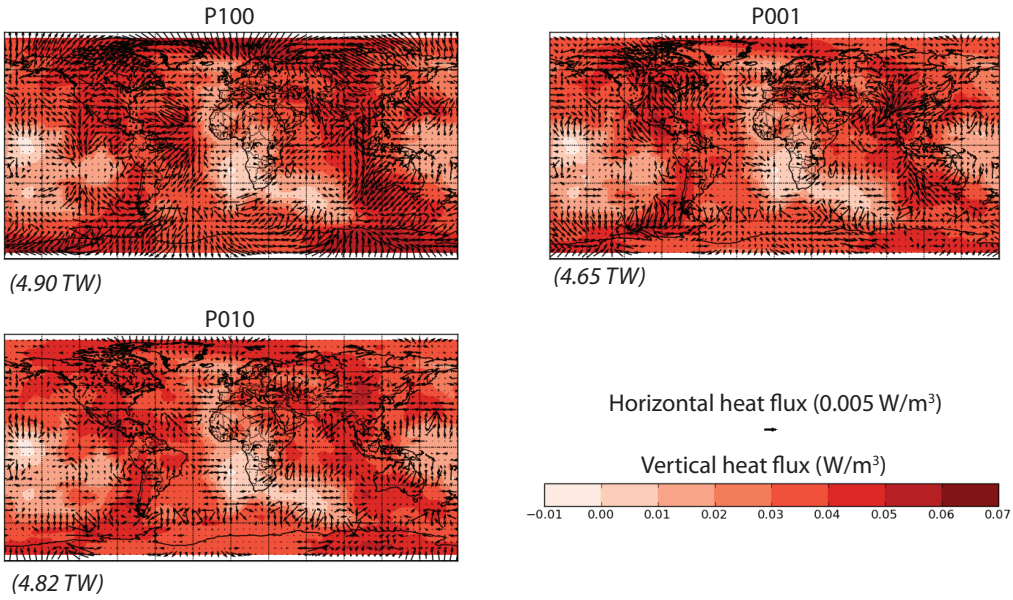

Figure 5: **CMB heat flux for various anisotropic models of thermal conductivity in a mixed-phase variable temperature lowermost mantle.** Scale and symbols are identical to Figure 3 but, for the cold post-perovskite areas, the thermal conductivity is anisotropic and derived from three different models of the activities of post-perovskite slip systems.

References

1. S. Stackhouse, L. Stixrude, and B. B. Karki. Thermal conductivity of MgO and $MgSiO_3$ perovskite at lower mantle conditions. *EOS: Transactions of the American Geophysical Union*, Fall meeting supplement:abstract number MR13C–05, 2009.

2. M. Murakami, K. Hirose, K. Kawamura, N. Sata, and Y. Ohishi. Post-perovskite phase transition in $MgSiO_3$. *Science*, 304:855 – 858, 2004.

3. A. R. Oganov and S. Ono. Theoretical and experimental evidence for a post-perovskite phase of $MgSiO_3$ in Earth's D″ layer. *Nature*, 430:445 – 448, 2004.

4. A. R. Oganov, J. P. Brodholt, and G. D. Price. Comparative study if quasiharmonic lattice dynamics, molecular dynamics and Debye model applied to $MgSiO_3$ perovskite. *Physics of the Earth and Planetary Interiors*, 122:277–288, 2000.

5. F. D. Stacey and P. M. Davis. *Physics of the Earth*. Cambridge University Press, fourth edition, 2008.

6. L. Stixrude and C. Lithgow-Berelloni. Thermodynamics of mantle minerals – ii. phase equilibria. *Geophysical Journal International*, 184:1180 – 1213, 2011.

7. A. M. Walker, A. M. Forte, J. Wookey, A. Nowacki, and J.-M. Kendall. Elastic anisotropy of D″ predicted from global models of mantle flow. *Geochemistry Geophysics Geosystems*, 12:Q10006, 2011.

8. N. A. Simmons, A. M. Forte, and S. P. Grand. Joint seismic, geodynamic and mineral physical constraints on three-dimensional mantle heterogeneity: Implications for the relative importance of thermal versus compositional heterogeneity. *Geophysical Journal International*, 177:1284 – 1304, 2009.

9. R. Taylor. Thermal diffusivity of composits. *High Pressures – High Temperatures*, 15:299 – 309, 1983.

10. J. X. Mitrovica and A. M. Forte. A new inference of mantle viscosity based upon joint inversion of convection and glacial isostatic adjustment data. *Earth and Planetary Science Letters*, 225:177 – 189, 2004.

11. A. M. Forte. Constraints on seismic models from other disciplines – implications for mantle dynamics and composition. In B. Romanowicz and A. Dziewonski, editors, *Treatise on Geophysics. Seismology and the Structure of the Earth*, volume 1, pages 805 – 858. Elsevier, 2007.

12. R. A. Lebensohn and C. N. Tomé. A self-consistent anisotropic approach for the simulation of plastic deformation and texture development of polycrystals: Application to zirconium alloys. *Acta Metallurgica et Materialia*, 41:2611 – 2624, 1993.

13. C. N. Tomé and G. R. Canova. Self-consistent modeling of heterogeneous plasticity. In U. F. Kocks, C. N. Tomé, and H.-R. Wenk, editors, *Texture and Anisotropy. Preferred Orientations in Polycrystals and their Effect on Materials Properties*, pages 466 – 511. Cambridge University Press, 1998.

14. S. Merkel, A. K. McNamara, A. Kubo, S. Speziale, L. Miyagi, Y. Meng, T. S. Duffy, and H.-R. Wenk. Deformation of (Mg,Fe)SiO_3 post-perovskite and D" anisotropy. *Science*, 316:1729 – 1732, 2007.

15. P. Carrez, D. Ferré, and P. Cordier. Implications for plastic flow in the deep mantle from modelling dislocations in $MgSiO_3$ minerals. *Nature*, 446:68 – 70, 2007.

16. P. Carrez, D. Ferré, and P. Cordier. Peierls-Nabarro model for dislocations in $MgSiO_3$ post-perovskite calculated at 120 GPa from first principles. *Philosophical Magazine*, 87:3229 – 3247, 2007.

17. L. Miyagi, W. Kanitpanyacharoen, P. Kaercher, K. K. M. Lee, and H.-R. Wenk. Slip systems in $MgSiO_3$ post-perovskite: implications for D″ anisotropy. *Science*, 329:1636 – 1638, 2010.